RSC Advances

PAPER

View Article Online
View Journal | View Issue



Cite this: *RSC Adv.*, 2016, **6**, 38653

# Glucose-assisted transformation of Ni-doped-ZnO@carbon to a Ni-doped-ZnO@void@$SiO_2$ core–shell nanocomposite photocatalyst†

Qiaoqiao Yin,‡[a] Wenjie Wu,‡[a] Ru Qiao,*[a] Xiaoxia Ke,[a] Yong Hu[b] and Zhengquan Li*[b]

Carbon-coated nickel-doped-ZnO nanorods (Ni/ZnO@C NRs) are successfully prepared for the purpose of improving the visible-light photocatalytic performance of ZnO by expanding the absorption in the visible-light region and increasing the separation efficiency of photogenerated charges. The physicochemical properties of the catalysts were characterized using SEM, TEM, XRD, and Raman, FT-IR, UV-vis diffuse reflectance and PL spectra. The results indicated that nickel ions substituted for $Zn^{2+}$ in the lattice of ZnO, whereas all the carbon was uniformly coated on the surface of the nanorod photocatalysts. Among the Ni/ZnO@C samples with different ion-doping levels and carbon coating content, the 1.0 mol% Ni/ZnO@C-3 sample possessing a carbon layer thickness of 3.8 nm exhibited a higher visible light activity and synergistic effects of the nickel and carbon, which were responsible for improving the photocatalytic activity. By using the hydrothermal carbon layer as a sacrificial template, nanovoid core–shell structured Ni/ZnO@void@$SiO_2$ was obtained through subsequent silica coating and calcination reactions. Its porous shell could adsorb dye molecules from the bulk solution and accumulate them in the void space where the Ni/ZnO core is more accessible than for the bare Ni/ZnO nanorods in bulk solution, meanwhile the nanovoid structure could also avoid shielding of the catalyst-active sites by the outer layer, which leads to a significant photocatalytic activity enhancement. In addition, antibacterial studies of Ni/ZnO@void@$SiO_2$ under sunlight irradiation were performed against *Escherichia coli*. This nanovoid photocatalyst exhibited high inhibition of the Gram-negative bacterial strain with co-action of the surface adsorption of the mesoporous $SiO_2$ and the strong oxidation abilities of the formed reactive oxygen species.

Received 13th December 2015
Accepted 7th April 2016

DOI: 10.1039/c5ra26631a

www.rsc.org/advances



## Introduction

Semiconductor-assisted photocatalysis has attracted considerable attention because it is one of the promising tools for solving environmental problems through the photochemical degradation of organic contaminants.[1–3] Among various photocatalysts being investigated, ZnO has been widely accepted as suitable for use due to its high redox potential, superior chemical stability, cost effectiveness, and nontoxicity. However, the application of pure ZnO is limited, because of its serious drawbacks of fast charge recombination and a finite visible-light absorption.[4] Therefore, significant efforts have been devoted to the improvement of the photocatalytic efficiency of ZnO in the visible-light region.[5–12] The doping of non-metals and transition metals is a very expedient way to convert ZnO into a sunlight-active photocatalyst, many dopants such as C, N, V, Mn, Co, and Ni have been used and have shown a better photocatalytic performance.[13–18]

However, when aiming to enhance the visible-light induced photocatalytic activity of ZnO, the preparation of ZnO with ion doping as the only effort to do so is far from enough. Generally, increase of the surface area leads to improvement of the photocatalytic activity, which can be concluded from the Langmuir–Hinshelwood mechanism. Recently, amorphous carbon has been reported to be an efficient coating material for improvement of the solar absorption ability, photocorrosion resistance, or electronic properties of the coated materials.[19–22] It can be easily obtained *via* an inexpensive and environmentally friendly hydrothermal or solvothermal process, simply using glucose as a precursor. Furthermore, carbonaceous materials can act as sacrificial templates or support shells for the synthesis of hollow nanostructures, yolk–shell nanostructures and other complex nanostructures.[9,23–26]

Therefore, aiming at constructing a novel visible-light photocatalyst, the design and fabrication of a core (ion-doped-ZnO)@shell (carbon) nanocomposite can make use of its unique

[a]*College of Chemistry and Life Sciences, Zhejiang Normal University, Jinhua 321004, China. E-mail: qiaoru@zjnu.cn*

[b]*Institute of Physical Chemistry, Zhejiang Normal University, Jinhua 321004, China*

† Electronic supplementary information (ESI) available: SEM, EDS, UV-vis DRS, XPS, PL, TGA, detection of ROS species and scheme for the reaction mechanism. See DOI: 10.1039/c5ra26631a

‡ These authors contributed equally to this manuscript.

advantages of impeding the photocorrosion of ZnO-type catalysts and enhance their photostability. In the present work, Ni/ZnO@C photocatalysts were prepared *via* a facile and green two-step hydrothermal route involving zinc acetate and glucose as precursors for ZnO and carbon. The photocatalytic experimental results showed that the as-obtained Ni/ZnO@C nanocomposites exhibited highly enhanced photocatalytic activity, which can be ascribed to the existence of strong interactions between the highly disordered carbon layer and the Ni/ZnO nanorods (NRs).

Furthermore, we also aimed to create a void layer between the semiconductor core and the porous shell to obtain a phase-selective photocatalyst because this structure can not only benefit the mass transfer of the reactants through the porous medium, but also can avoid the active sites of the photocatalyst being shielded by a coating layer directly. Therefore, through a two-step reaction consisting of silica coating and high-temperature calcination, the Ni/ZnO@C core–shell NRs were transformed to Ni/ZnO@void@$SiO_2$ core–shell NRs which exhibited even better photocatalytic activities and an antibacterial effect.

## Experimental section

### Preparation of Ni-doped-ZnO (Ni/ZnO) nanorods

In a typical process, $Zn(Ac)_2 \cdot 2H_2O$ (4.95 mmol), $Ni(Ac)_2 \cdot 2H_2O$ (0.05 mmol) and SDS (0.3 g) were successively dissolved in 30 mL of $CH_3OH$ and the mixture was stirred for 60 min. NaOH (0.8 g, 20 mmol) was added to the above solution with continuous stirring to form a homogeneous solution. After stirring for 30 min, the suspension was transferred to a Teflon-lined stainless steel autoclave of 40 mL capacity and kept at 140 °C for 4 h. After the reaction, the autoclave was cooled to room temperature naturally, and the Ni/ZnO nanorods were centrifuged and washed with DI water and ethanol.

### Preparation of the Ni/ZnO@C core–shell structure

0.2 g of the as-prepared Ni/ZnO nanorods was dispersed in 24 mL of $C_2H_5OH$ using ultrasonication to form a suspension. 8 mL of an aqueous solution containing 0.5 g of glucose was added into the above suspension under gentle stirring. This mixed suspension was transferred into a 40 mL autoclave, and maintained at 180 °C for 6 h. Finally, the solid product was collected by centrifugation, washed with deionized water and absolute ethanol, then dried in an oven at 80 °C for 2 h, which was denoted as Ni/ZnO@C-1. On altering the amount of glucose to 0.75, 1.00 and 1.50 g, the other as-obtained products were denoted as Ni/ZnO@C-2, Ni/ZnO@C-3 and Ni/ZnO@C-4, respectively.

### Preparation of Ni/ZnO@void@$SiO_2$

Firstly, Ni/ZnO@C@$SiO_2$ composites were prepared using a modified Stöber method.[27,28] The above-mentioned Ni/ZnO@C nanorods were dispersed in a mixed solution containing 80 mL $H_2O$, 60 mL ethanol, 0.30 g CTAB and 1 mL $NH_3 \cdot H_2O$. After ultrasonication for 30 min, 200 μL of TEOS was added, and the mixture was vigorously stirred at room temperature for 6 h. The precipitate was harvested by centrifugation, and washed with distilled water three times and with ethanol three times, then dried at 80 °C for 4 h.

Finally, a Ni/ZnO@void@$SiO_2$ rodlike photocatalyst was obtained by calcining the above-described Ni/ZnO@C@$SiO_2$ at 500 °C under an air atmosphere for 4 h in a furnace. The heating rate from room temperature to 500 °C was 10 °C $min^{-1}$.

### Characterization

The crystallographic structures of the samples were studied with powder X-ray diffraction (XRD, Philips PW3040/60). The structures and compositional information of the samples were studied using scanning electron microscopy (SEM, Hitachi S-4800), transmission electron microscopy (TEM, Hitachi H-7500) and high-resolution transmission electron microscopy (HRTEM, JEOL JEM-2100F). Raman spectra were acquired using a confocal Raman Witec alpha 300 SR with an excitation laser at 488 nm. Photoluminescence spectra were obtained at room temperature on a Hitachi F-7000 fluorescence spectrophotometer. The absorption spectra were obtained using a PerkinElmer Lambda 900 UV-vis spectrophotometer. Thermogravimetric analysis (TGA) of the products was performed on a Netzsch STA 449C thermal analyzer. $N_2$ adsorption–desorption isotherms were collected using a Micrometrics ASAP 2020 surface area and porosity analyzer at 77 K, after the sample had been degassed with vacuum and $N_2$ flushing, at 120 °C for 4 h.

### Photocatalytic tests

The photoefficiencies of all the synthesized catalysts were evaluated through degradation of a RhB aqueous solution under visible light irradiation. In a typical experiment, 20 mg of the photocatalyst was dispersed in 100 mL of a 5 mg $L^{-1}$ RhB solution. After stirring in the dark for a fixed time to reach the adsorption–desorption equilibrium, the suspension was exposed to a 300 W Xe lamp equipped with a 420 nm cut-off filter with stirring. During the experiment, 5 mL samples of the suspension were taken at 30 min intervals and centrifuged for subsequent RhB absorbance analysis. The change in the RhB absorbance of the solution was used to monitor the extent of the degradation at given time intervals.

### Evaluation of antibacterial activity

For the antibacterial experiments, *Escherichia coli* (*E. coli*, ATCC 25922, Gram-negative bacterium) was selected as an indicator species. All culture vessels, tubes and materials were sterilized in an autoclave before use. The photocatalytic antibacterial activity of Ni/ZnO@void@$SiO_2$ against *E. coli* was validated using a spread plate method.[29] The spread plate method is a quantitative method which shows the viability of the bacterial cells after incubation in culture vessels. In the experiment, the photoinactivation of bacteria was studied by mixing 5 mg of the Ni/ZnO@void@$SiO_2$ agent in 8 mL of a nutrient broth containing $1 \times 10^8$ CFU $mL^{-1}$ of *E. coli*. Firstly, the suspension was magnetically stirred for 30 min under dark conditions, which was followed by taking 200 μL of the mixed solution out and

 

spreading it on a nutrient agar plate. Then, the suspension was exposed to sunlight irradiation with stirring. After each 10 min interval, a 200 μL aliquot was taken out and spread on an agar plate. In addition, 200 μL of suspended bacterial cells without the antibacterial agent served as a control was also spread over a nutrient agar plate. Finally, all the spread agar plates were incubated at 37 °C for 18 h and then the number of bacterial colonies was counted.

## Results and discussion

As we know, the presence of excess transition metal ions during a solvothermal process introduces excessive vacancies and even secondary phase impurities into the ZnO NRs, which can work as charge-carrier recombination centers, leading to an enhancement of the recombination of electron–hole pairs and a decrease of the charge carrier concentration, and finally reduction of the photocatalytic activity.[30] So the choosing of an appropriate Ni-doping concentration for preparation of the Ni/ZnO photocatalyst is one of the key factors affecting its photocatalytic efficiency. Fig. 1a shows XRD patterns of the as-prepared pure ZnO NRs and Ni/ZnO NRs with a varied doping content. As shown, the XRD patterns for all the samples reveal a mono-phasic hexagonal wurtzite structure indexed to the standard XRD data file of ZnO (JCPDS no. 36-1451), showing that the $Ni^{2+}$ ions occupied $Zn^{2+}$ sites in the wurtzite structure. The intensity of the diffraction peaks weakens with the increase of Ni content, which implies that the Ni-doping has the effect of inhibiting the crystallization of ZnO. It is also worth noting that there is a slight shift of the ZnO (002) peak to a higher angle (inset of Fig. 1a) for all the doped ZnO samples, which results from a contraction of the host lattice owing to the small difference in the ionic radius between the tetrahedrally coordinated zinc(II) (0.74 Å) and the nickel(II) (0.69 Å). The chemical state of Ni was further investigated using XPS (Fig. S1†). As shown in Fig. S1c,† the two main peaks of $Ni2p_{3/2}$ and $Ni2p_{1/2}$ lie at 854.8 eV and 872.4 eV, respectively, and their corresponding satellite peaks were also observed at 861.7 eV and 879.7 eV, which means that a charge transfer transition of O(2p) → Ni(3d) occurred, indicating that the Ni ions substituting for Zn ions were doped into the ZnO lattice and the chemical state of the Ni ions in the Ni/ZnO NRs was $Ni^{2+}$.[31,32] For comparison, SEM images of the as-prepared pure ZnO NRs and Ni/ZnO NRs with a different doping content are shown in Fig. S2.† It is obvious that the morphology of the Ni/ZnO NRs remained virtually unchanged as the dopant concentration increased.

The photocatalytic activities of the different samples were evaluated using photoassisted degradation of a RhB aqueous solution under visible light irradiation. As shown in Fig. 1b, the self-degradation of RhB, without involving a photocatalyst, was negligible. On comparison with pure ZnO synthesized through the same approach, the photodegradation performance of ZnO was increased by substituting $Ni^{2+}$ ions for $Zn^{2+}$ in the ZnO matrix and 1 mol% Ni/ZnO possessed the best photocatalytic activity. The enhanced degradation efficiency of the as-prepared Ni/ZnO NRs may be ascribed to the synergistic effects of $Ni^{2+}$ and ZnO. As displayed in the UV-vis diffuse reflectance spectra

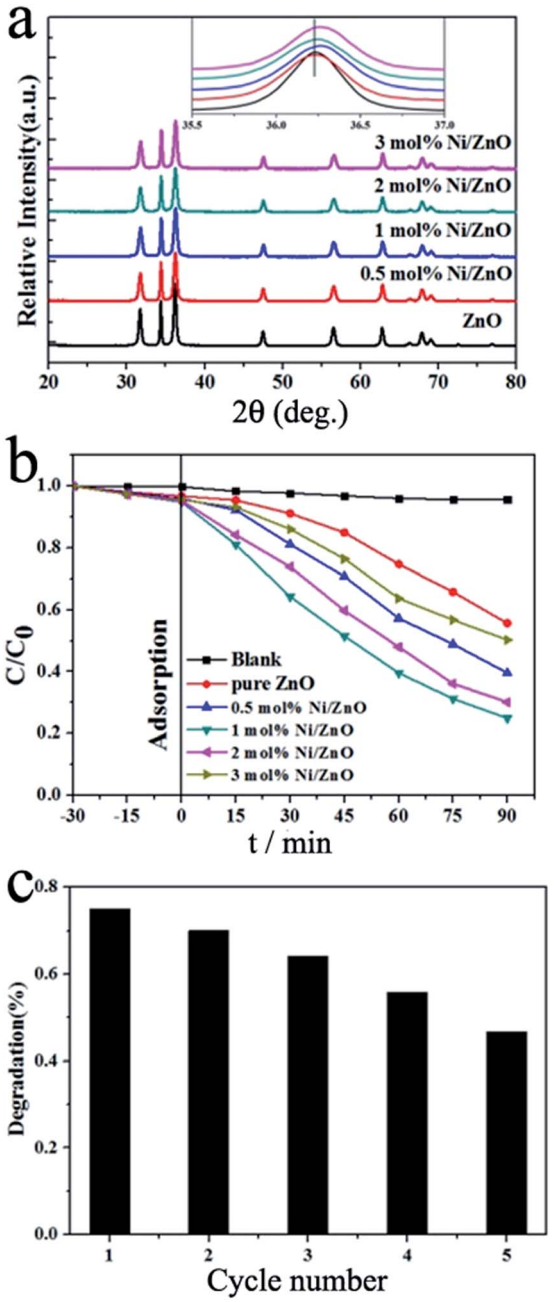


Fig. 1 (a) XRD patterns and (b) the photodegradation performance of Ni/ZnO NRs with different Ni-doping concentrations. (c) Recycling test for the degradation of RhB using 1 mol% Ni/ZnO as a photocatalyst under visible light irradiation.

of the samples prepared with different amounts of nickel (Fig. S3†), the more enhanced absorption observed in the visible light region can be attributed to $Ni^{2+}$-incorporation in the ZnO matrix, and the absorption intensity between 400 and 800 nm increases with increasing nickel content. This demonstrates that $Ni^{2+}$-incorporation can greatly enhance the photon absorption of Ni/ZnO in the region of visible light which can be utilized for photocatalytic reactions. Meanwhile, PL measurements were employed for further investigation of the photocatalytic activity of Ni/ZnO because the activity is related to the

PL intensity and the recombination rate of photoexcited electrons and holes. A reduced excitonic emission intensity was identified for the most active photocatalyst 1 mol% Ni/ZnO in comparison to undoped ZnO, which suggests that the Ni-doping could quench the fluorescence from the ZnO NRs (Fig. S4†). A lower photoluminescence intensity reflects a lower electron–hole recombination rate, and hence a longer lifetime of the photogenerated carriers, which are favorable for enhancing the photocatalytic activity of the semiconductor.[33] So the PL spectra show that the doped $Ni^{2+}$ ions, acting as mediators for interfacial charge transfer, could effectively inhibit electron and hole recombination during the photocatalytic reaction under visible light irradiation.

We also studied the photostability of the Ni/ZnO NRs by repeating for five cycles the photodegradation of RhB under visible light irradiation. The results shown in Fig. 1c indicate that the Ni/ZnO catalyst can be utilized repeatedly, but the marked reduction of the photocatalytic activity illustrates that the photostability of the doped ZnO should be further strengthened. Constructing a carbon-coated semiconductor core–shell structure is a means to achieve this one goal. In our follow-up synthesis of core–shell structured heterojunctions, the most active photocatalyst 1 mol% Ni/ZnO was used as the core material.

Fig. 2 shows typical SEM and TEM images of the Ni/ZnO@C core–shell NRs with the surface coated by an amorphous carbonaceous layer. The as-prepared Ni/ZnO@C nanorods were about 30 nm in diameter with a range of 200–500 nm for the length (Fig. 2a and b). Besides, no by-products such as carbon spheres or particles were observed from the images, indicating that the carbonization of glucose was performed directly on the surface of the Ni/ZnO NRs. With increasing amounts of glucose, the shell thickness of the carbon layer increased gradually (Fig. 2c–f, Table 1). All the Ni/ZnO@C samples exhibited high Brunauer–Emmett–Teller (BET) specific surface areas (from 31.796 to 46.060 $m^2 g^{-1}$, Table 1). As an amorphous carbon layer can cause the scattering of X-rays,[19] a reduced diffraction intensity in the XRD patterns of all the core–shell samples can be observed (Fig. S5†).

A Raman spectrum of the Ni/ZnO@C material is shown in Fig. 3. The peak at 1367.5 $cm^{-1}$ is usually associated with the vibration of carbon atoms with dangling bonds for in-plane terminations of disordered graphite, and is labeled as the D band. The peak at 1591.4 $cm^{-1}$ (G band) indicates the presence of $sp^2$ hybridized graphite carbon. The results were used to further ascertain that the shells are carbon. TG analysis showed that the weight percent of the carbon content in the Ni/ZnO@C-1, Ni/ZnO@C-2, Ni/ZnO@C-3 and Ni/ZnO@C-4 NRs was 8.8%, 17.0%, 22.0 wt% and 26.7%, respectively (Fig. S6†). The carbon layer makes it difficult to distinguish the spectrum of the wurtzite Ni/ZnO for the core–shell NRs due to attenuation of the Raman signals, so the Raman spectrum of the Ni/ZnO NRs was further recorded at a low wave number range.[34,35] The inset of Fig. 3 shows the Raman spectra of non-carbon-coated Ni/ZnO NRs and undoped ZnO NRs in the 1200 to 200 $cm^{-1}$ wave number range. The sharpest and strongest peak at ~434 $cm^{-1}$ can be attributed to the nonpolar high-frequency optical phonon branch of the $E_2$ mode ($E_{2H}$), which involves the motion of oxygen and is characteristic of a wurtzite structure.[36–38] The peaks at 323 and 378.5 $cm^{-1}$ were assigned to the second-order vibration mode and the $A_1$(TO) mode, respectively. The weak peaks located at 544, 580, and 666 $cm^{-1}$ can be assigned to 2LA, $A_1$(LO) and $2(E_2H–E_2L)$[39] higher-order Raman vibrational modes, respectively. In addition, in the high-wave number region, the peak at 1144 $cm^{-1}$ can be attributed to contributions of the $2A_1$(LO) and $2E_1$(LO) modes.[40] Compared with the undoped ZnO, the position of the vibrational modes of Ni/ZnO has shifted slightly to a higher wavelength, and the intensity decreased due to the formation of structure defects and local lattice distortions induced by doping.[41–43]

The formation of Ni/ZnO@C core–shell NRs was also investigated using FT-IR, for which the FT-IR spectra are shown in Fig. 4. The characteristic peak at *ca.* 500 $cm^{-1}$ is assigned to the stretching vibration of Zn–O for the Ni-doped ZnO. The peaks at *ca.* 3500, 1700 and 1600 $cm^{-1}$ are assigned to the stretching vibration of O–H and the stretching vibrations of C–O and C=O of $COO^-$ groups, respectively, which reflect the aromatization and incomplete carbonization of glucose.[44,45] In comparison with the uncoated Ni/ZnO sample, the C=O and O–H peaks for all the Ni/ZnO@C samples increase remarkably in intensity, and show a shift in the absorption wavelength, implying interaction between the Ni/ZnO and carbon in the Ni/ZnO@C.[21]

The optical properties of the Ni/ZnO@C samples were determined with the help of UV-vis spectrophotometry at room temperature. As shown in Fig. 5, all of the spectra exhibit a representative and intense peak in the UV region (~410 nm) due to the band gap transition of the ZnO semiconductor. Additional absorption is observed in the visible light region. Compared to the uncoated Ni/ZnO NRs, all the carbon-coated samples show enhanced visible absorption. However, Ni/ZnO@C-4 shows a weaker visible light absorption than Ni/ZnO@C-3, and the absorption intensity drops faster especially at longer wavelengths. The above results illustrate that a thick carbon layer would increase the diffuse reflectivity and deteriorate the light absorption ability of the photocatalyst. Therefore, controlling the thickness of the carbon layer is of critical importance in the construction of sun-light activated photocatalysts.

The photocatalytic performance of the Ni/ZnO@C composites was evaluated by photodegrading a RhB solution under visible light illumination (Fig. 6). Obviously, all of the Ni/ZnO@C composites exhibit better photocatalytic activities than the non-carbon-coated Ni/ZnO (Fig. 6a). This is because the amorphous carbon layer with oxygen-containing groups can enhance the adsorption capability for organic dyes in comparison to uncoated Ni/ZnO. So in the reaction process, more of the photogenerated holes produced in the Ni/ZnO can be consumed by the dye molecules adsorbed on the Ni/ZnO surface rapidly, thus enhancing the photocatalytic activities of the Ni/ZnO@C NRs. At the same time, the carbon layer successfully prolongs the lifetime of photogenerated electron–hole pairs, improves the visible absorption ability, and enlarges the specific surface area, all of which result in the acceleration of photocatalytic reactions. The Ni/ZnO@C-3 sample shows the best

 

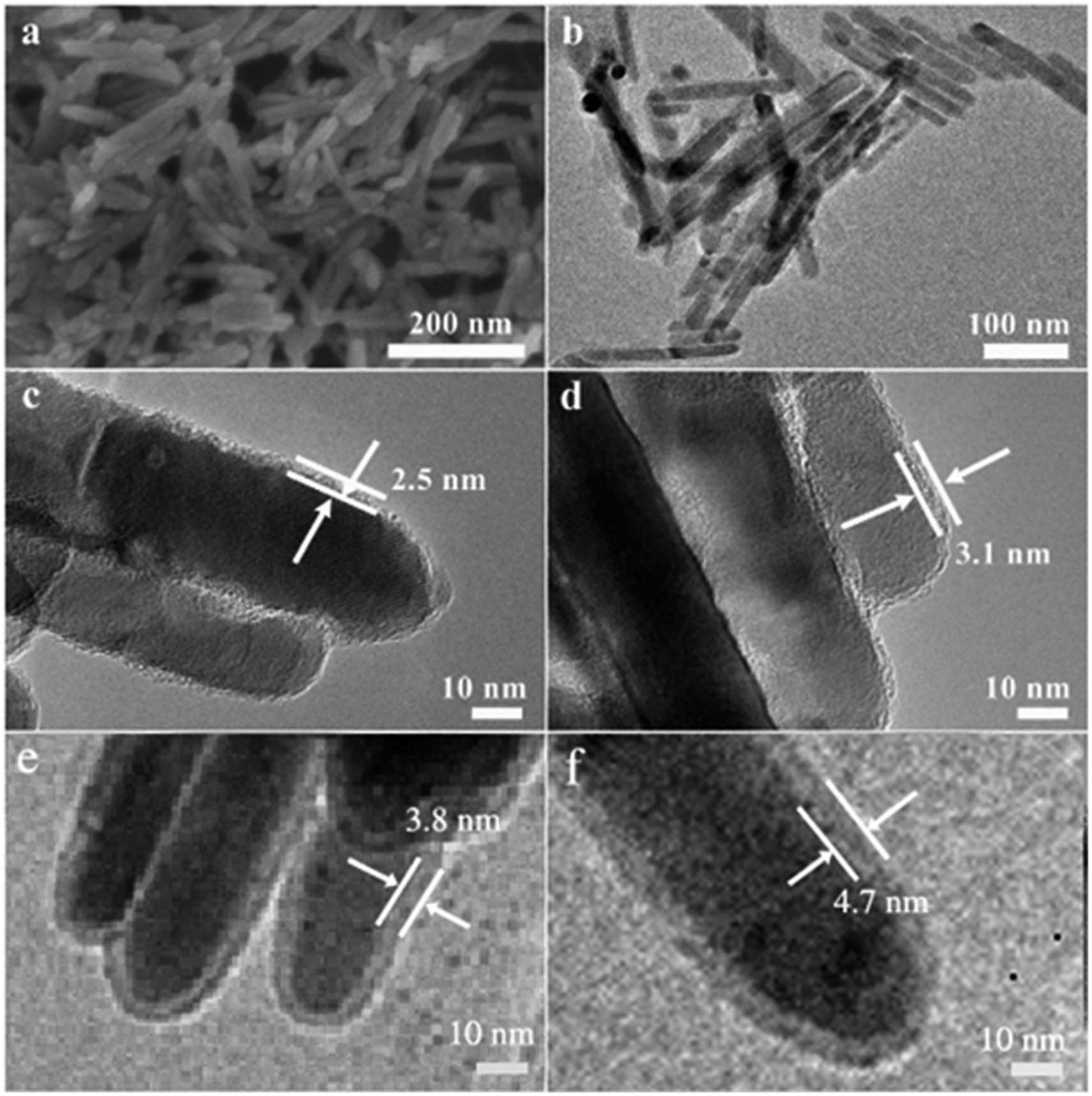


Fig. 2 (a) SEM and (b) TEM images of Ni/ZnO@C core–shell NRs prepared with 1.00 g of glucose. (c)–(f) HRTEM images of Ni/ZnO@C NRs prepared with different amounts of glucose: (c) 0.50 g, (d) 0.75 g, (e) 1.00 g and (f) 1.50 g.

Table 1 Surface properties of the Ni/ZnO@C NRs prepared with different amounts of glucose

| Sample | Amount of glucose (g) | Carbon layer[a] (nm) | BET surface area ($m^2$ $g^{-1}$) |
|---|---|---|---|
| Ni/ZnO@C-1 | 0.50 | 2.5 | 31.796 |
| Ni/ZnO@C-2 | 0.75 | 3.1 | 39.299 |
| Ni/ZnO@C-3 | 1.00 | 3.8 | 46.060 |
| Ni/ZnO@C-4 | 1.50 | 4.7 | 40.192 |

[a] The thickness of the carbon layer was calculated based on HRTEM images.

photocatalytic performance, evidenced by the fact that nearly 100% of the RhB was degraded in 90 min. Further increasing the mass ratio of glucose leads to a decrease in the photocatalytic activity, which is in agreement with the UV-vis results discussed above. The stability and reusability of Ni/ZnO@C

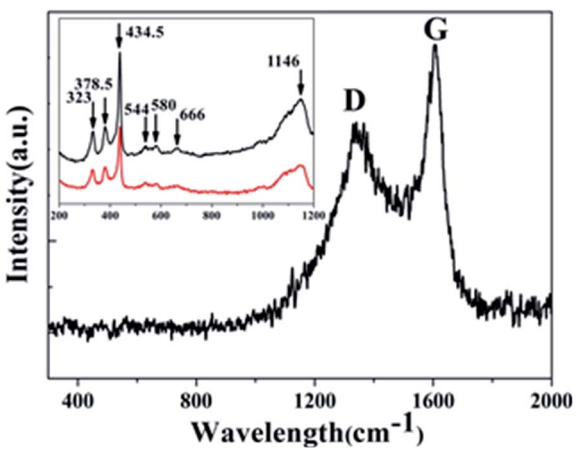


Fig. 3 Raman spectrum of the Ni/ZnO@C-3 sample. Inset: Raman spectra of non-coated Ni/ZnO NRs (red) and pure ZnO NRs (black).

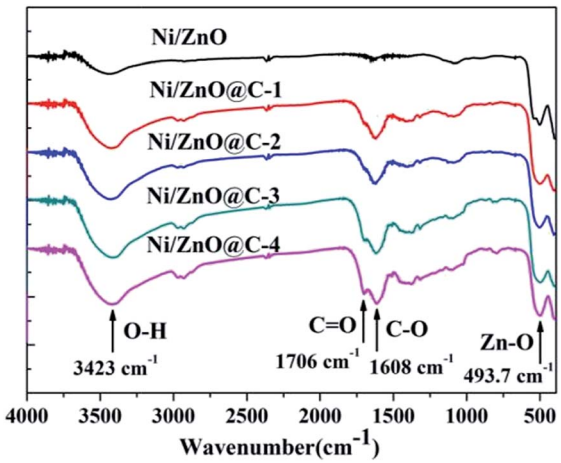


Fig. 4 FT-IR spectra of the as-prepared Ni/ZnO@C and Ni/ZnO NRs.

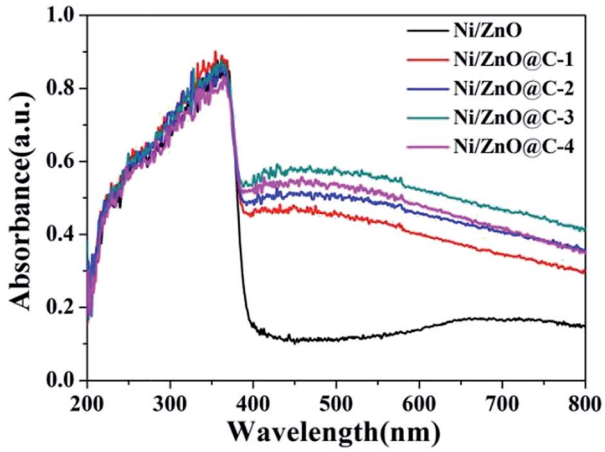


Fig. 5 UV-vis spectra of the Ni/ZnO@C and Ni/ZnO samples.

were evaluated by recollecting and reusing the Ni/ZnO@C-3 composite catalyst, and the results are shown in Fig. 6b. Ni/ZnO@C-3 exhibits excellent photostability with the decomposition ratio remaining at over 90% even after six cycles. This suggests that the photostability of the Ni/ZnO@C composite has been improved by the carbon coating layer on the doped semiconductor surface.

As compared with core–shell structures, a yolk–shell structure usually possesses a larger specific surface area, and the void space within the shell can provide a unique confined space for the yolk material to participate in confined catalysis, drug release, lithium-ion batteries, *etc.*[24,46,47] So yolk–shell structured materials can be regarded as nanoreactors for catalytic and photocatalytic reactions.[26,48] Here, Ni/ZnO@void@$SiO_2$ core–shell NRs with a nanovoid between the Ni/ZnO core and the $SiO_2$ layer, similar to a yolk–shell structure, were prepared using a hydrothermal carbon layer as a sacrificial template. The formation process for the Ni/ZnO@void@$SiO_2$ NRs is shown in Scheme 1. The XRD pattern of these core–shell NRs with a void structure (Fig. 7) indicates that the Ni/ZnO core was still maintained during the Stöber process, and that there was a diffraction signal in the $2\theta$ range of 10–30°, which could be attributable to amorphous silica.

The morphology of the Ni/ZnO@void@$SiO_2$ was obtained using SEM and TEM images (Fig. 8). By comparison with the Ni/ZnO@C sample, the TEM image of Ni/ZnO@void@$SiO_2$ shows that the Ni/ZnO NRs are well coated with a coarse silica shell and a bright ringed void can be observed between the Ni/ZnO core and the silica layer with a relatively uniform thickness. The nitrogen physical adsorption–desorption isotherms and the corresponding pore size distribution for the sample are shown in Fig. 8c and d. The textural properties of Ni/ZnO@void@$SiO_2$ were investigated, and the BET specific surface area ($S_{BET}$) and

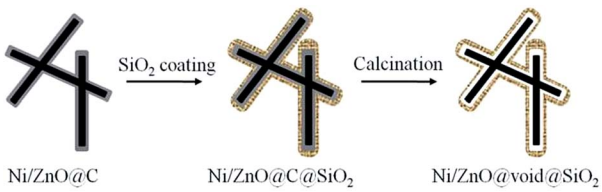


Scheme 1 Schematic illustration of the formation of Ni/ZnO@void@$SiO_2$ core–shell structured NRs.

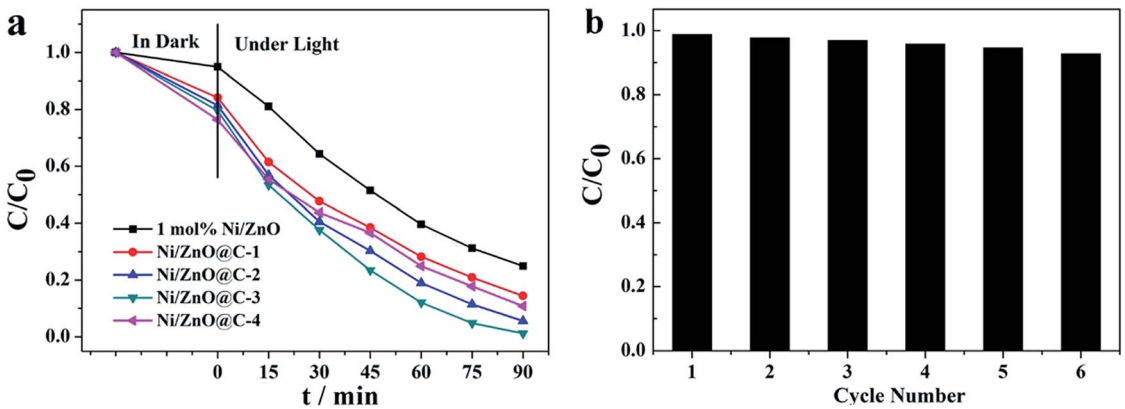


Fig. 6 (a) Photodegradation performance of the Ni/ZnO@C core–shell NRs prepared with different amounts of glucose. (b) Recycling test of Ni/ZnO@C-3 under visible light irradiation.

 

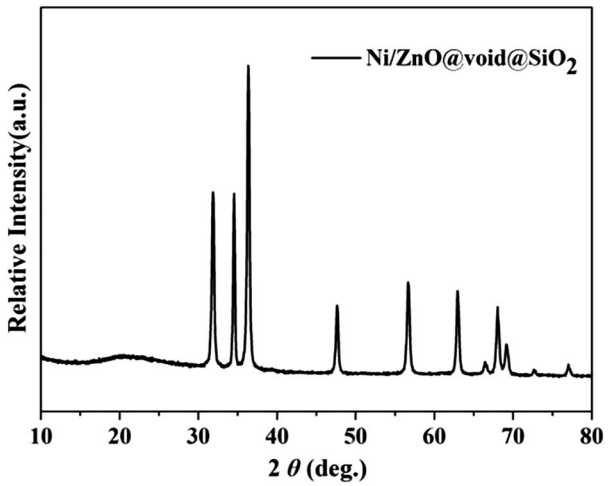


Fig. 7 XRD pattern of the Ni/ZnO@void@$SiO_2$ core–shell structure.

pore volume are 98.536 $m^2\ g^{-1}$ and 0.297 $cm^3\ g^{-1}$, respectively. In addition, compared with the pore size of Ni/ZnO@C, that of Ni/ZnO@void@$SiO_2$ increased sharply, from 7.6 nm to 106.2 nm (Table S1†), which can also prove the formation of a void inside Ni/ZnO@void@$SiO_2$. The sample displays a classical type IV isotherm with a type H3 hysteresis loop and shows a single modal pore size distribution in the microporous, mesoporous, and macroporous regions (Fig. 8d). After coating with a $SiO_2$ layer and removal of the carbon shell, the $S_{BET}$ increases and the pore size distribution peak gradually shifts to a larger pore region. This phenomenon might be interpreted as a consequence of diffusion of $CO_2$ caused by thermally induced combustion of the carbon-containing compounds. Therefore, the results of XRD, TEM, and nitrogen adsorption–desorption demonstrate that a Ni/ZnO@void@$SiO_2$ core–shell structure with a porous shell was successfully synthesized.

In comparison with the Ni/ZnO@C core–shell structured sample, Ni/ZnO@void@$SiO_2$ exhibits a stronger adsorption ability and a better photocatalytic activity. As shown in Fig. 9, after stirring in the dark to reach an adsorption–desorption equilibrium for the RhB molecules on the surface of the photocatalyst, the purple RhB solution could be turned to colorless in 60 min by catalytic oxidation with the Ni/ZnO@void@$SiO_2$ NRs under visible light irradiation. The outstanding activity of the photocatalyst with a nanovoid structure is attributed to the increased porosity of the $SiO_2$ shell created by removal of the carbon layer during the combustion process and the nanoreactor features of the nanovoid structure. The formed porous shell structure is beneficial for mass transfer of the reactants, so Ni/ZnO@void@$SiO_2$ can adsorb RhB molecules from the bulk solution and accumulate them in the void space, resulting in a higher reactant concentration in the void space. Furthermore, a striking feature of the nanovoid structure is that the calcination treatment avoids direct shielding of the active sites of the Ni/ZnO core by the silica coating, and the Ni/ZnO core keeps its

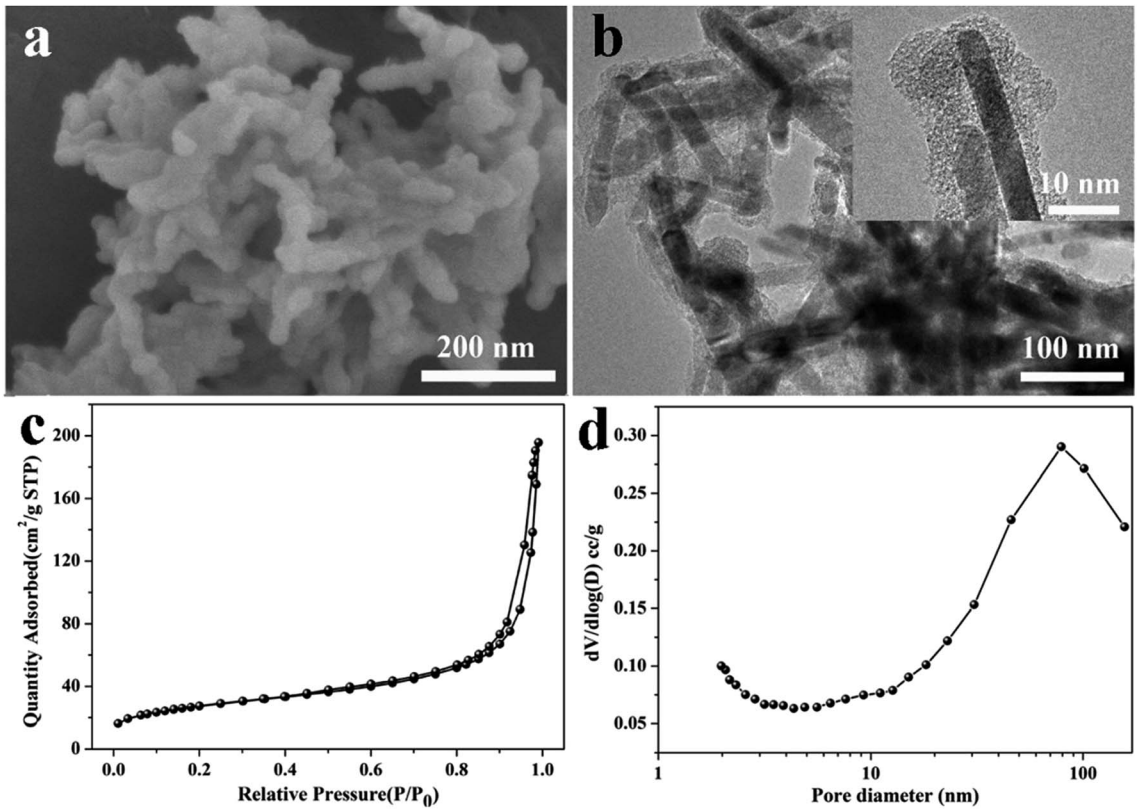


Fig. 8 (a) SEM and (b) TEM images of the Ni/ZnO@void@$SiO_2$ core–shell structure. (c) $N_2$ adsorption–desorption isotherms and (d) a pore-size distribution curve for Ni/ZnO@void@$SiO_2$.

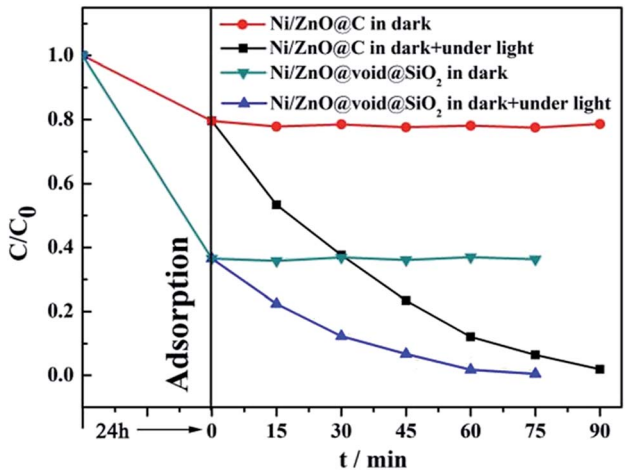


Fig. 9 Photocatalytic degradation of RhB under visible light using Ni/ZnO@C and Ni/ZnO@void@$SiO_2$ as catalysts.

inherent active sites for photocatalytic decomposition, which leads to a significant photocatalytic activity enhancement.

To investigate the main reactive species generated from the Ni/ZnO@void@$SiO_2$ NRs, ethylene diaminetetraacetic acid (EDTA), tertiary butanol (*t*-BuOH) and benzoquinone (BQ) were used as scavengers for $h^+$, $^{\bullet}OH$ and $^{\bullet}O_2^-$ in the degradation experiments. Fig. S7a† displays the photocatalytic activities of the Ni/ZnO@void@$SiO_2$ NRs after adding the different scavengers. With EDTA or BQ, the degradation rate for the RhB solution was only slightly reduced compared with that of the control experiment without scavenger. These results suggest that both $h^+$ and $^{\bullet}O_2^-$ are not the major reactive species. In the presence of *t*-BuOH, however, the degradation rate was greatly reduced, revealing that $^{\bullet}OH$ radicals are the dominant reactive species. To confirm this hypothesis, we also introduced a photoluminescence technique using terephthalic acid (TA) as a probe to further restrain the formation of $^{\bullet}OH$ radicals in the system.[49,50] As shown in Fig. S7b,† the characteristic peak of TAOH increases along with the irradiation time, indicating the continuous generation of $^{\bullet}OH$ radicals from the suspension. This result confirms that $^{\bullet}OH$ radicals are the main reactive species generated from the Ni/ZnO@void@$SiO_2$ NRs under visible light irradiation. A specific photodegradation mechanism for the Ni/ZnO@void@$SiO_2$ NRs under visible light is depicted in Scheme S1.†

The application of Ni/ZnO@void@$SiO_2$ as an antibacterial agent was demonstrated under sunlight illumination for a short time of 20 min to confirm its photocatalytic antibacterial effect owing to its special nanovoid structure. The antibacterial activity of Ni/ZnO@void@$SiO_2$ against *E. coli* is illustrated in Fig. 10. From the plate assay, it was observed that the control experiment (absence of antibacterial agent) showed no inhibition of the bacterial growth. But when the Ni/ZnO@void@$SiO_2$ agent was present in the bacterial suspension, even when the suspension was treated under dark conditions, the colony forming units of bacteria were significantly reduced in the agar plate (Fig. 10b), which indicates that the presence of the nanovoid product in the bacterial solution inhibits the bacterial

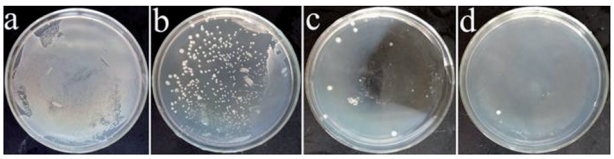


Fig. 10 Photographs of the colony forming units of viable *E. coli* (a) in the absence of antibacterial agent (control), (b) treated with the Ni/ZnO@void@$SiO_2$ agent under dark conditions, and (c) and (d) treated with the Ni/ZnO@void@$SiO_2$ agent and exposed to sunlight irradiation for 10 min and 20 min, respectively.

growth. Fig. 10c and d show photoinactivation of the bacteria in the presence of Ni/ZnO@void@$SiO_2$ at different intervals of irradiation time. Interestingly, it was found that the antibacterial effect of the nanovoid product was higher under sunlight irradiation than in the dark, and its antibacterial rate increased with increasing irradiation. Almost 100% of the bacteria were killed after 20 min irradiation in the presence of 0.625 mg $mL^{-1}$ photocatalyst.

It is possible that the antibacterial activity of Ni/ZnO@void@$SiO_2$ is due to a collapsing of the cells by a force generated by reactive oxygen species (ROS). By using $KBrO_4$ and tertiary butanol as scavengers for $^{\bullet}OH$ and $^{\bullet}O_2^-$ radicals in the photocatalytic antibacterial test, respectively, it can be confirmed that both of these oxygen radicals play crucial roles in this process. As shown in Fig. S8b and d,† an increased concentration of $KBrO_4$ trapped more of the produced $^{\bullet}OH$, which resulted in a decrease of the antibacterial activity of the photocatalyst. Similarly, the results shown in Fig. S9† exhibit that the trapping of $^{\bullet}O_2^-$ also led to a decrease of the antibacterial activity of Ni/ZnO@void@$SiO_2$. As illustrated in Scheme S1,† under sunlight irradiation, photoinduced electron–hole pairs ($e^-$–$h^+$) are generated in the Ni/ZnO nanorods. $h^+$ can efficiently react with surrounding $H_2O$ molecules (or $OH^-$) to produce $^{\bullet}OH$ radicals. At the same time, $e^-$ are scavenged by dissolved oxygen molecules to yield $^{\bullet}O_2^-$. Finally, both of the reactive oxygen species exhibit a collapsing force which leads to bacterial death.

## Conclusions

In summary, these are first results demonstrating a glucose-assisted transformation of Ni/ZnO@C to a Ni/ZnO@void@$SiO_2$ core–shell rod-like photocatalyst. The porous structure of the $SiO_2$ layer is beneficial for mass transfer of the reactants and accumulating them in the void space. Meanwhile, the void structure lying between the Ni/ZnO (core) and $SiO_2$ (shell) can protect the inherent active sites of Ni/ZnO for the photodecomposition of organic pollutants. Thus, the Ni/ZnO@void@$SiO_2$ heterogeneous photocatalyst shows an even better catalytic performance than uncoated Ni/ZnO and Ni/ZnO@C materials. In addition, this nanovoid photocatalyst shows antibacterial activity against a microbial pathogen (*E. coli*). Photoinactivation of the bacteria in the presence of sunlight was more effective than exposure to the catalyst material under dark conditions.

 

## Acknowledgements

This work is financially supported by the National Natural Science Foundation of China (Grant No. 21201151, 21273203), the Natural Science Foundation of Zhejiang Province (Grant No. LY15B010003) and the Open Research Fund of Jiangsu Key Laboratory of Environmental Material and Environmental Engineering (Grant No. K13069).

## References

1 M. A. Fox and M. T. Dulay, *Chem. Rev.*, 1993, **93**, 341–357.
2 M. R. Hoffmann, S. T. Martin, W. Y. Choi and D. W. Bahnemann, *Chem. Rev.*, 1995, **95**, 69–96.
3 A. Mills and S. L. Hunte, *J. Photochem. Photobiol., A*, 1997, **108**, 1–35.
4 M. Romero, J. Blanco, B. Sánchez, A. Vidal, S. Malato, A. I. Cardona and E. Garcia, *Sol. Energy*, 1999, **66**, 169–182.
5 S. Cho, J. W. Jang, J. S. Lee and K. H. Lee, *Langmuir*, 2010, **26**, 14255–14262.
6 P. Li, Z. Wei, T. Wu, Q. Peng and Y. D. Li, *J. Am. Chem. Soc.*, 2011, **133**, 5660–5663.
7 C. L. Yu, K. Yang, Y. Xie, Q. Z. Fan, J. C. Yu, Q. Shu and C. Y. Wang, *Nanoscale*, 2013, **5**, 2142–2151.
8 C. L. Yu, K. Yang, W. Q. Zhou, Q. Z. Fan, L. F. Wei and J. C. Yu, *J. Phys. Chem. Solids*, 2013, **74**, 1714–1720.
9 J. Mu, C. Shao, Z. Guo, Z. Zhang, M. Zhang, P. Zhang, B. Chen and Y. Liu, *ACS Appl. Mater. Interfaces*, 2011, **3**, 590–596.
10 C. Eley, T. Li, F. L. Liao, S. M. Fairclough, J. M. Smith, G. Smith and S. C. E. Tsang, *Angew. Chem., Int. Ed.*, 2014, **53**, 7838–7842.
11 C. L. Yu, K. Yang, Q. Shu, J. C. Yu, F. F. Cao and X. Li, *Chin. J. Catal.*, 2011, **32**, 555–565.
12 N. C. S. Selvam, J. J. Vijaya and L. J. Kennedy, *Ind. Eng. Chem. Res.*, 2012, **51**, 16333–16345.
13 S. W. Liu, C. Li, J. G. Yu and Q. J. Xiang, *CrystEngComm*, 2011, **13**, 2533–2541.
14 H. C. Qin, W. Y. Li, Y. J. Xia and T. He, *ACS Appl. Mater. Interfaces*, 2011, **3**, 3152–3156.
15 W. Yu, H. F. Liu, L. Zhang, H. X. Gao and G. S. Fu, *Phys. Status Solidi B*, 2010, **247**, 2185–2189.
16 Y. C. Lu, Y. H. Lin, T. F. Xie, S. L. Shi, H. M. Fan and D. J. Wang, *Nanoscale*, 2012, **4**, 6393–6400.
17 S. Kuriakose, B. Satpati and S. Mohapatra, *Phys. Chem. Chem. Phys.*, 2014, **16**, 12741–12749.
18 Q. Yin, R. Qiao, Z. Li, X. L. Zhang and L. Zhu, *J. Alloys Compd.*, 2015, **618**, 318–325.
19 Y. Guo, H. S. Wang, C. L. He, L. J. Qiu and X. B. Cao, *Langmuir*, 2009, **25**, 4678–4684.
20 P. Zhang, C. H. Shao, Z. Y. Zhang, M. Y. Zhang, J. B. Mu, Z. C. Guo and Y. C. Liu, *Nanoscale*, 2011, **3**, 2943–2949.
21 P. Zhang, B. B. Li, Z. B. Zhao, C. Yu, C. Hu, S. J. Wu and J. S. Qiu, *ACS Appl. Mater. Interfaces*, 2014, **6**, 8560–8566.
22 L. W. Zhang, H. Y. Cheng, R. L. Zong and Y. F. Zhu, *J. Phys. Chem. C*, 2009, **113**, 2368–2374.
23 Z. W. Deng, M. Chen, G. X. Gu and L. M. Wu, *J. Phys. Chem. B*, 2008, **112**, 16–22.
24 Y. Cheng, X. Y. Niu, T. Y. Zhao, F. L. Yuan, Y. J. Zhu and H. G. Fu, *Eur. J. Inorg. Chem.*, 2013, 4988–4997.
25 Z. W. Zhang, Y. M. Zhou, Y. W. Zhang, S. J. Zhou, J. J. Shi, J. Kong and S. C. Zhang, *Dalton Trans.*, 2013, **42**, 5004–5012.
26 Z. M. Cui, Z. Chen, C. Y. Cao, L. Jiang and W. G. Song, *Chem. Commun.*, 2013, **49**, 2332–2334.
27 M. Xu, R. Qiao, X. L. Zhang, Y. S. Kang and L. C. Li, *Mater. Lett.*, 2012, **66**, 285–288.
28 Y. H. Deng, D. W. Qi, C. H. Deng, X. M. Zhang and D. Y. Zhao, *J. Am. Chem. Soc.*, 2008, **130**, 28–29.
29 S. Singh, K. C. Barick and D. Bahadur, *CrystEngComm*, 2013, **15**, 4631–4639.
30 K. C. Barick, S. Singh, M. Aslamb and D. Bahadur, *Microporous Mesoporous Mater.*, 2010, **134**, 195–202.
31 Y. M. Liu, T. Wang, X. Sun, Q. Q. Fang, Q. R. Lv, X. P. Song and Z. Q. Sun, *Appl. Surf. Sci.*, 2011, **257**, 6540–6545.
32 X. T. Wang, L. P. Zhu, L. Q. Zhang, J. Jiang, Z. G. Yang, Z. Z. Ye and B. He, *J. Alloys Compd.*, 2011, **509**, 3282–3285.
33 Y. Hu, X. H. Gao, L. Yu, Y. R. Wang, J. Q. Ning, S. J. Xu and X. W. D. Lou, *Angew. Chem., Int. Ed.*, 2013, **52**, 5636–5639.
34 E. Markevicha, R. Sharabia, O. Haika, V. Borgela, G. Salitraa, D. Aurbacha, G. Semraub, M. A. Schmidtb, N. Schallc and C. J. Stinnerc, *Power Sources*, 2011, **196**, 6433–6439.
35 X. Wang, H. Q. Fan, P. R. Ren and M. M. Li, *RSC Adv.*, 2014, **4**, 10284–10289.
36 T. C. Damen, S. P. S. Porto and B. Tell, *Phys. Rev.*, 1966, **142**, 570.
37 C. A. Arguello, D. L. Rousseau and S. P. S. Porto, *Phys. Rev.*, 1969, **181**, 1351.
38 J. M. Calleja and M. Cardona, *Phys. Rev. B: Solid State*, 1977, **16**, 3753.
39 S. J. Chen, Y. C. Liu, C. L. Shao, R. Mu, Y. M. Lu, J. Y. Zhang, D. Z. Shen and X. W. Fan, *Adv. Mater.*, 2005, **17**, 586–590.
40 R. Cuscó, E. Alarcón-Lladó, J. Ibáñez, L. Artús, J. Jiménez, B. G. Wang and M. J. Callahan, *Phys. Rev. B: Condens. Matter Mater. Phys.*, 2007, **75**, 165202–165211.
41 X. Wang, J. Xu, B. Zhang, H. Yu, J. Wang, X. Zhang, J. Yu and Q. Li, *Adv. Mater.*, 2006, **18**, 2476–2480.
42 M. Schumm, M. Koerdel, S. Müller, H. Zutz, C. Ronning, J. Stehr, D. M. Hofmann and J. Geurts, *New J. Phys.*, 2008, **10**, 043004.
43 A. Singhal, S. N. Achary, J. Manjanna, S. Chatterjee, P. Ayyub and A. K. Tyagi, *J. Phys. Chem. C*, 2010, **114**, 3422–3430.
44 X. M. Sun and Y. D. Li, *Angew. Chem., Int. Ed.*, 2004, **43**, 597–601.
45 S. K. Li, F. Z. Huang, Y. Wang, Y. H. Shen, L. G. Qiu, A. J. Xie and S. J. Xu, *J. Mater. Chem.*, 2011, **21**, 7459–7466.
46 Y. F. Zhu, T. Ikoma, N. Hanagata and S. Kaske, *Small*, 2010, **6**, 471–478.
47 J. Liu, S. Z. Qiao, J. S. Chen, X. W. Lou, X. R. Xing and G. Q. Lu, *Chem. Commun.*, 2011, **47**, 12578–12591.
48 S. Wang, T. Wang, W. X. Chen and T. Hori, *Chem. Commun.*, 2008, 3756–3758.
49 K. Ishibashi, A. Fujishima, T. Watanabe and K. Hashimoto, *Electrochem. Commun.*, 2000, **2**, 207–210.
50 F. Ahmed, N. Arshi, M. S. Anwar, R. Danish and B. H. Koo, *RSC Adv.*, 2014, **4**, 29249–29263.